Optimized Reactive Power Flow of DFIG Power Converters for Better Reliability Performance Considering Grid Codes

Zhou, Dao; Blaabjerg, Frede; Lau, Mogens; Tonnes, Michael

Published in:
I E E E Transactions on Industrial Electronics

DOI (link to publication from Publisher):
10.1109/TIE.2014.2359911

Publication date:
2015

Optimized Reactive Power Flow of DFIG Power Converters for Better Reliability Performance Considering Grid Codes

Dao Zhou, *Student Member, IEEE*, Frede Blaabjerg, *Fellow, IEEE*, Mogens Lau and Michael Tonnes

***Abstract* – If there is no reactive power exchange between the Doubly-Fed Induction Generator (DFIG) and the grid, the various characteristics of the power converters in the DFIG wind turbine system cause the lifetime expectancy of the rotor-side converter significantly less than the grid-side converter. In order to fulfill the modern grid codes, over-excited reactive power injection will further reduce the lifetime of the rotor-side converter. In this paper, the additional stress of the power semiconductor due to the reactive power injection is firstly evaluated in terms of modulation index and the current loading. Then an optimized reactive power flow is proposed in the case an over-excited reactive power support is applied with the joint compensation from both the rotor-side converter and the grid-side converter. Finally, some experimental validations are performed at a down-scale DFIG prototype. It is concluded that, among the different combined reactive power support strategies, the best scheme will trade-off the lifetime between the grid-side converter and the rotor-side converter.**

***Index Terms* – Doubly-fed induction generator, reactive power, thermal behavior, consumed lifetime.**

I. INTRODUCTION

The worldwide wind capacity reached close to 320 GW by the end of the 2013 [1]. As the modern wind turbine is required to act like the conventional synchronous generator with independent reactive power and active power regulation in order to handle the power quality issues [2], the power electronics are nowadays playing a more and more important role even to the full-scale of the wind turbine generator (e.g. permanent-magnet synchronous generator). In order to reduce the cost of the wind power generation, the power rating of the wind turbine is now up-scaling to 8 MW. However, the feedback of the wind turbine market indicates that the best-seller is still those rated around 2-3 MW, in which the Doubly-Fed Induction Generator (DFIG) is normally employed together with the partial-scale power electronic converters [3]-[6].

Another progress in the wind turbine technology is the movement of wind farms from onshore to offshore to reduce the environment impact and also obtain even better wind conditions. Because of the expensive maintenance for the offshore wind farms, the lifetime of the whole system preserves normally 20-25 years, much longer than the traditional industrial standard [7]. Consequently, the reliability of the offshore wind turbine system becomes of interest from the manufacturer's perspective. As the-state-of-art agreement, the reliability engineering in power electronics is currently moving from a solely statistical approach to a more physics based approach, which involves not only the statistics but also the root cause behind the failures [8]-[13].

Considerable reliability tests have already been carried out by the leading power semiconductor manufacturers. In [14], [15], the power cycles of the power device are provided in traction systems from a thermal stress point of view, and the most important factors affecting the lifetime are summarized in [16] (e.g. mean junction temperature, junction temperature fluctuation, on-state time duration of a periodical current, etc.). A lot of papers also address the reliability issues in wind turbine systems [17]-[20], which implies that the thermal cycles of the power semiconductor generally include the small cycles (e.g. current commutation within one fundamental frequency) and the large cycles (e.g. the fluctuation of wind speed and environment temperature). This paper mainly focuses on the steady-state small thermal cycles. In the DFIG system, as the Rotor-Side Converter (RSC) and the Grid-Side Converter (GSC) are both able to provide the reactive power support, thereby the total minimum power can be achieved by using a proper reactive power share, which can enhance the system efficiency [21], [22]. Moreover, due to the various characteristics of the power converters in the DFIG system, it can also be seen that the lifetime expectancy between the RSC and the GSC could also be significantly unequal. This paper investigates a smart reactive power share between the Back-to-Back (BTB) power converters in order to balance their lifetime seen from the thermal stress of the power semiconductor.

The layout of this paper is organized as follows. In section II, the loss breakdown and the thermal behavior of the power device are estimated at some typical wind speeds, thus the consumed lifetime of the power converters can be obtained based on an annual wind profile. Section III describes the additional stress of the power device introduced by the reactive power support required by the modern grid codes. In

Manuscript received November 18, 2013; revised March 8, 2014, June 11, 2014 and July 30, 2014; accepted August 31, 2014.

Section IV, as the reactive power can be supplied either from the GSC or the RSC, different combined reactive power compensation strategies are adopted in order to seek the best solution for the DFIG system in respect to the lifetime expectancy of the power converters. In Section V, the experimental results of the reactive power compensation strategies are tested in a down-scale DFIG system. Finally, some conclusions are drawn in Section VI for controlling this system.

II. Various Characteristics of BTB Power Converters in Respect to Reliability

The typical configuration of the DFIG based wind turbine system is shown in Fig. 1. As the BTB power converters have different performances (e.g. the control objectives, the interface voltages and the operational frequencies), different loss distributions in the power semiconductors can be expected, thus various thermal profiles inevitably induce an unbalanced lifetime between the GSC and the RSC. Based on a typical annual wind profile, this section will evaluate the estimated lifespan of the power electronic converters.

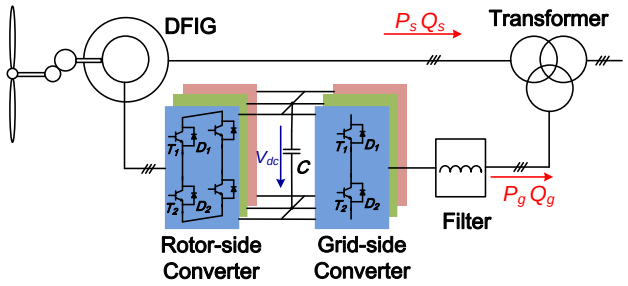

Fig. 1. Doubly-fed induction generator-based wind energy generation system.

A. Loss breakdown of power device

The power loss of the power device mainly includes the conduction loss and the switching loss [23]. The conduction loss in each power device P_{con} can be deduced as [24],

$$P_{con} = f \cdot (\sum_{n=1}^{N} v_{CE}(|i_a(n)|) \cdot |i_a(n)| \cdot T_1(n) + \sum_{n=1}^{N} v_F(|i_a(n)|) \cdot |i_a(n)| \cdot (T_s - T_1(n))) \quad (1)$$

where the first term is the conduction loss of the IGBT T_{con}, and the second term is the conduction loss of the freewheeling diode D_{con}. i_a is the sinusoidal current through the power device, T_1 is the ON time of the upper leg within a switching period T_s (in Fig. 1), v_{CE}, v_F are voltage drops of the IGBT and the diode during their on-state period, which are normally given by the manufacturer. N is the carrier ratio, whose value is the switching frequency over the fundamental frequency f, and the subscript n is the nth switching pattern.

The space vector modulation is widely used in a three-phase three-wire system due to its higher utilization of the DC-link voltage. In order to guarantee the minimum harmonic, the symmetrical sequence arrangement of the no-zero vector and zero-vector is normally used, and the conduction time of the upper and the lower switch of leg can thus be deduced based on the voltage angle [25]. Within one fundamental frequency of the converter output current, each IGBT in a leg always conducts only half period. The direction of the current is relevant to the conduction loss distribution between the IGBT and the diode. As a result, the phase angle between the converter voltage and the current is also important.

For the RSC, the phase angle is related to the power factor of the stator-side of the DFIG as well as the DFIG instinctive parameters. Neglecting the stator resistance and the rotor resistance, the steady-state DFIG equivalent circuit is shown in Fig. 2 in terms of the phasor expression.

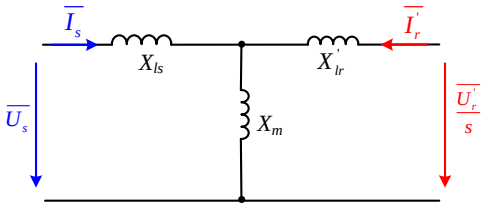

Fig. 2. One phase DFIG equivalent circuit in phasor diagram.

Taking phase A as an example, if the stator voltage is assumed as the reference direction and all quantities are transferred to the stator side, the voltage and current relationship between the rotor-side and the stator-side are,

$$\overline{I_r'} = -\frac{X_s}{X_m} I_{s\_Re} + j \cdot sign(s) \cdot (-\frac{U_{s\_Re}}{X_m} - \frac{X_s}{X_m} I_{s\_Im}) \quad (2)$$

$$\overline{U_r'} = s \cdot (\frac{X_r}{X_m} U_{s\_Re} + \frac{\sigma X_r X_s}{X_m} I_{s\_Im}) - j \cdot (sign(s)) \cdot (s \frac{\sigma X_r X_s}{X_m} I_{s\_Re}) \quad (3)$$

where X_s, X_m and X_r denote the stator reactance, the magnetizing reactance and the rotor reactance, respectively. σ is the leakage coefficient, defined as $(X_sX_r-X_m^2)/X_sX_r$. s is the slip value of the induction generator. Moreover, the sign function $sign(s)$ means if s is positive, its value becomes 1. Alternatively, if s is negative, its value becomes -1.

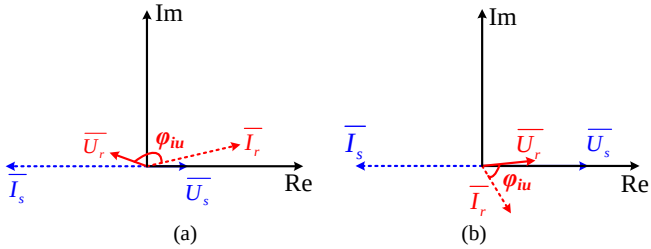

Fig. 3. Phasor diagram of the stator voltage, stator current and rotor voltage, rotor current. (a) Super-synchronous mode; (b) Sub-synchronous mode.

According to (2) and (3), the phasor diagram of the stator voltage, stator current and rotor voltage, rotor current is then shown in Fig. 3. In the super-synchronous mode, the rotor voltage is almost in an opposite phase in respect to the stator voltage, as the slip value is negative. Moreover, the rotor current is almost lagging the rotor voltage 180°, which indicates that the DFIG provides the active power through the

rotor-side, and the RSC also supplies the excitation energy for the induction generator. In the sub-synchronous mode, the rotor current is lagging the rotor voltage less than 90°, implying that the RSC provides both the active power and the reactive power to the induction generator.

For the GSC, if a single inductance is used as filter as shown in Fig. 4, by definition of the grid voltage as the reference, the voltage and current relationship between the grid and the converter output are,

$$\overline{I_g} = I_{g\_\mathrm{Re}} + jI_{g\_\mathrm{Im}} \tag{4}$$

$$\overline{U_C} = U_{g\_\mathrm{Re}} - X_g \cdot I_{g\_\mathrm{Im}} + j(-X_g \cdot I_{g\_\mathrm{Re}}) \tag{5}$$

where X_g denotes the filter reactance. The phasor diagram of the grid-side converter voltage and current is shown in Fig. 5.

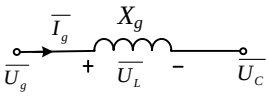

Fig. 4. One phase L filter of the grid-side converter in phasor diagram.

The switching loss in each power device P_{sw} can be calculated as,

$$P_{sw} = \frac{U_{dc}}{U_{dc}^*} \cdot f \cdot \left(\sum_{n=1}^{N} \left(E_{on}(|i_a(n)|) + E_{off}(|i_a(n)|)\right) + \sum_{n=1}^{N} E_{rr}(|i_a(n)|)\right) \tag{6}$$

Similarly as (1), the first term is the switching loss for the IGBT T_{sw}, and the second term is the switching loss for the freewheeling diode D_{sw}. E_{on} and E_{off} are the turn-on and the turn-off energy dissipated by the IGBT, and E_{rr} is the reverse-recovery energy dissipated by the diode, which are normally tested by the manufacturer at certain DC-link voltage U_{dc}^*. It is assumed that the switching energy is proportional to the actual DC-link voltage U_{dc}.

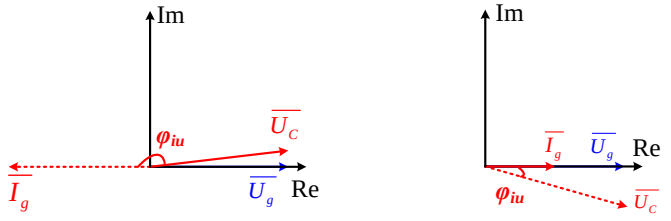

Fig. 5. Phasor diagram of the grid-side converter output voltage and current. (a) Super-synchronous mode; (b) Sub-synchronous mode.

A 2 MW wind turbine system is used as a case study, and its parameters are listed in Appendix. With the aid of the conventional vector control, the maximum power point tracking is used for the active power reference. If no reactive power compensation is taken into account, the loss breakdown of each power device can be analytically evaluated in terms of the RSC and the GSC, as shown in Fig. 6.

B. Thermal cycling of power device

Thermal impedance that decides the junction temperature of the power device usually consists of the thermal parameters of the power module itself (from junction to baseplate or case), and Thermal Integrate Material (TIM) as well as the cooling method, as shown in Fig. 7.

Generally, the thermal time constant of a typical air cooling system is from dozens of seconds to hundreds of seconds for MW-level power converter, while the maximum thermal time constant of the power device is hundreds of milliseconds. On the other hand, the maximum fundamental period of the power converters output current is only one second, which implies that the thermal cycling caused by the air cooling can almost be neglected [26], [27]. As a result, for the steady-state power cycle analysis, the thermal model of the cooling method will only affect the mean junction temperature, but not disturb the junction temperature fluctuation.

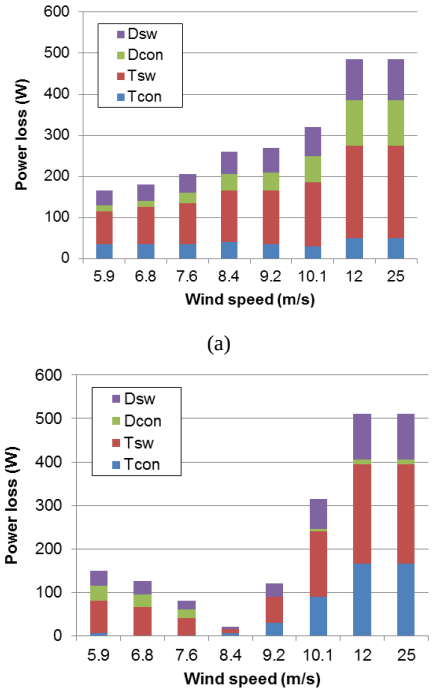

Fig. 6. Loss breakdown of each power device. (a) Rotor-side converter; (b) Grid-side converter.

As the mean junction temperature T_{jm} and the junction temperature fluctuation dT_j are commonly regarded as the two most important reliability assessment indicators, the formulae of them are [28],

$$T_{jm\_T/D} = P \cdot \sum_{i=1}^{4} R_{thjc\_T/D(i)} + P \cdot \sum_{j=1}^{3} R_{thca\_(j)} + T_a \tag{7}$$

$$dT_{j\_T/D} = 2P \cdot \sum_{i=1}^{4} R_{thjc\_T/D(i)} \cdot \frac{\left(1 - e^{-\frac{t_{on}}{\tau_{thjc\_T/D(i)}}}\right)^2}{1 - e^{-\frac{t_p}{\tau_{thjc\_T/D(i)}}}} \tag{8}$$

In (7), R_{thjc} is the thermal resistance from the junction to case of the power module, R_{thca} is the thermal resistance of the

air cooling, in which subscripts T and D denote the IGBT and the freewheeling diode, whereas subscripts i and j denote four-layer and three-layer Foster structure for power module and air cooling, respectively. P is the power loss of each power semiconductor, and T_a is the ambient temperature. In (8), t_{on} denotes the on-state time within each fundamental period of current at the steady-state operation, t_p denotes the fundamental period of the current, τ denotes the each Foster layer's thermal time constant.

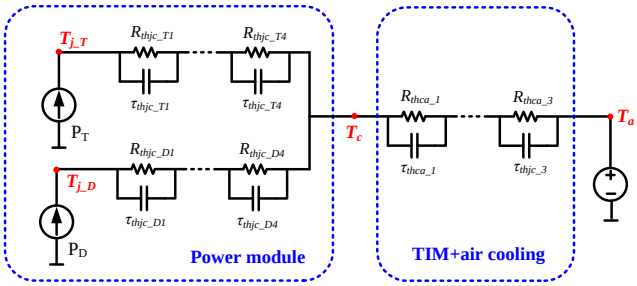

Fig. 7. Thermal model of power semiconductor for power cycles induced by the fundamental frequency.

C. Estimated lifetime based on annual wind profile

Power cycling test is defined that the power components are actively heated up by the losses in the semiconductor and cooled down again with the aid of cooling system. This test can detect the thermo-mechanical stress between the layers with different thermal expansion coefficients, in which the connection between the chip and Direct Bonded Copper (DBC) and bond wire connection seems to be the most frequent failure mechanisms [14], [15], [26].

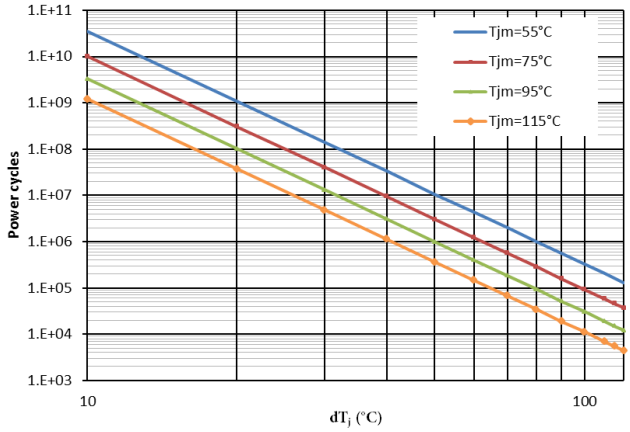

Fig. 8. Example of fitting power cycles curve versus the mean junction temperature and the junction temperature fluctuation according to Coffin-Mansion model [16].

In order to accelerate the testing, the introduced current almost equals the rated current of the power semiconductor, and the time cycling is normally between some seconds to dozens of seconds. The values of the power cycles can be obtained at higher junction temperature fluctuations, and then the values at lower temperature variation can be extrapolated by the Coffin-Mansion equation [16]. Based on the simplified assumption of the uniform failure mechanism over the entire temperature range, the B10 lifetime (10% of sample components fail if power cycles reach the B10 value) is shown in Fig. 8 with various mean junction temperatures and various junction temperature fluctuations.

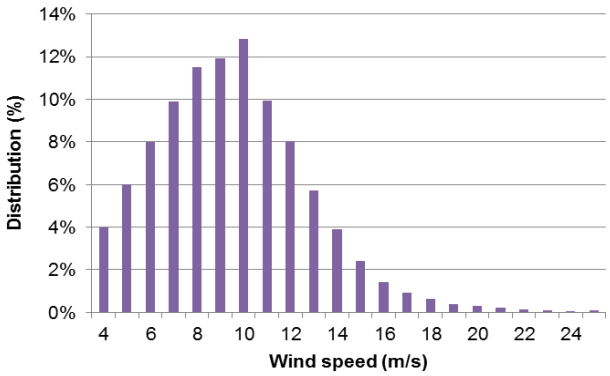

Fig. 9. Class I annual wind profile according to IEC standard [33], [34].

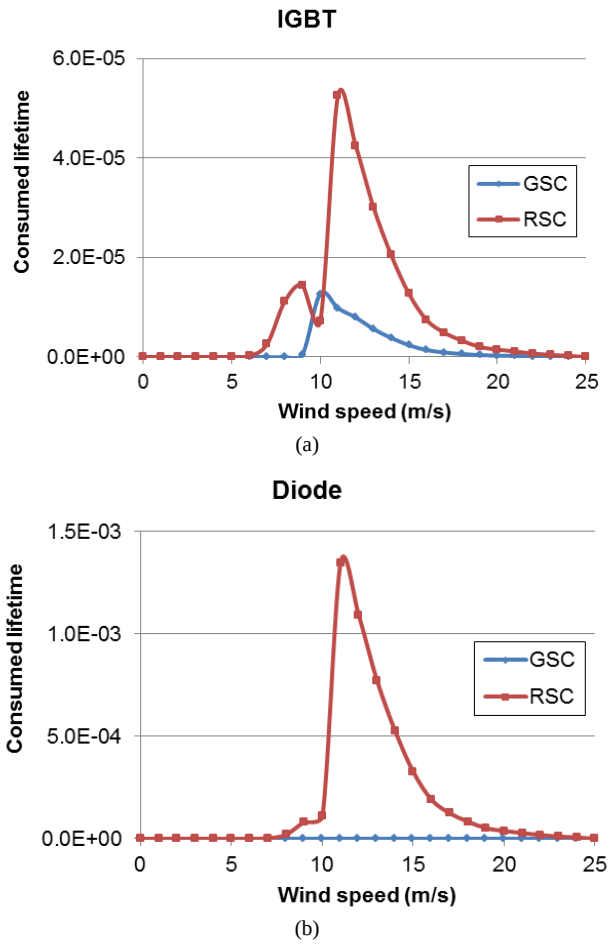

Fig. 10. Consumed lifetime of the switching semiconductors in the back-to-back power converters at each wind speed if the reactive power is zero. (a) IGBT; (b) Diode.

Note: GSC denotes the grid-side converter, and RSC denotes the rotor-side converter.

Based on (7) and (8), as well as Fig. 6, the steady-state mean junction temperature and junction temperature

fluctuation can be calculated at each individual wind speed. Together with a Class I annual wind speed distribution shown in Fig. 9, in which the velocity increment is 1 m/s, the individual B10 power cycles can be obtained from the cut-in wind speed of 4 m/s to the cut-off wind speed of 25 m/s. Besides, it is worth to mention the rated wind speed of 11 m/s.

The lifetime consumed per year of the IGBT and freewheeling diode inside the BTB power converters at each wind speed can be calculated as,

$$CL_m = D_m \cdot \frac{365 \cdot 24 \cdot 3600 \cdot f_m}{N_m} \tag{9}$$

where D is the annual percentage of every wind speed, f is the fundamental frequency of the output current, and N is the power cycles consistent with Fig. 8. Subscript m denotes the various wind speed from the cut-in to the cut-off wind speed.

The lifetime consumed per year of the IGBT and freewheeling diode are thus shown in Fig. 10(a) and Fig. 10(b). For the RSC, it can be seen that the diode dominates the lifetime compared to the IGBT, while for the GSC, it is the IGBT that has much less lifetime expectancy. Moreover, the lifespan of the RSC is much shorter than the GSC.

According to the Miner's rule [17], [19], [29], the total consumed lifetime per year can then be estimated by,

$$CL = \sum_{m=4}^{25} CL_m \tag{10}$$

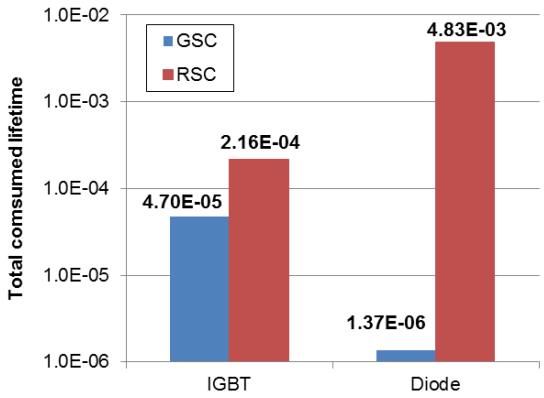

Fig. 11.Total consumed lifetime between the rotor-side converter and the grid-side converter.

A comparison of the total consumed lifetime between the RSC and the GSC is shown in Fig. 11. It is noted that the lifetime of the BTB power converters becomes very unbalanced, in which the lifetime of the GSC only consumes 1/100 of the RSC. Moreover, due to the orders of magnitude difference between the IGBT and the diode in respect to the total consumed lifetime, for simplicity, the thermal performance of the diode is only focused to estimate the RSC lifetime, while only the IGBT is focused to analyze the lifespan for the GSC.

III. Lifetime Reduction to Support Modern Grid Codes

As the wind farms are normally located at the remote areas, stricter grid codes are issued in order to guarantee a stable grid voltage. This section will firstly describe a modern grid code, and then address the additional stress of the power device in respect to the reactive power injection.

A. Modern grid codes

As shown in Fig. 12, the most representative grid code in respect to the reactive power regulation is the E.ON requirement for grid connections [30]. If the active power is above 20%, up to 30% of the under-excited reactive power and 40% of the over-excited reactive power are expected to be supported. For the DFIG configuration, it is worth to note that the under-excited reactive power denotes reactive power absorbed from the grid by the DFIG. Alternatively, the over-excited reactive power denotes the reactive power injected to the grid by the DFIG.

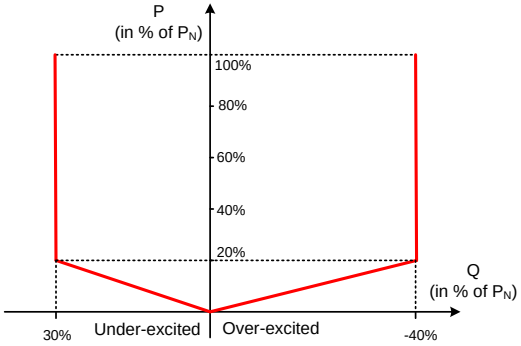

Fig. 12. Reactive power support stated in the German grid code [30].

B. Reactive power stress on BTB power converters

For the RSC, as illustrated in (2) and (3), the rotor current and the rotor voltage of the DFIG is closely related to the generated active power by the wind energy, as well as the reactive power exchange between the DFIG and the grid required by the transmission system operator. Similarly, for the GSC, it can be seen from (4) and (5) that the converter current and its interfacing voltage also depend on the active power and reactive power. As a result, the supportive reactive current introduces additional current stress to the power device as well as the voltage stress in DC-link voltage for both the RSC and the GSC [27]. As these two factors are tightly linked to the loss dissipation of the power semiconductor, the effects of the reactive power injection on the current and voltage stress of the power device are shown in Fig. 13(a) and Fig. 13(b), respectively, where the wind speeds 12 m/s, 8.4 m/s and5.9 m/s indicate the super-synchronous mode, synchronous mode and sub-synchronous mode of the DFIG operation.

For the GSC, the modulation index almost reaches 1.0 at three typical wind speeds when there is no reactive power exchange between the DFIG and the grid. The synchronous mode has the relatively minimum value due to the very small slip power through the power converter. Moreover, the over-excited reactive power stresses the DC-link voltage significantly, while the under-excited reactive power reliefs,

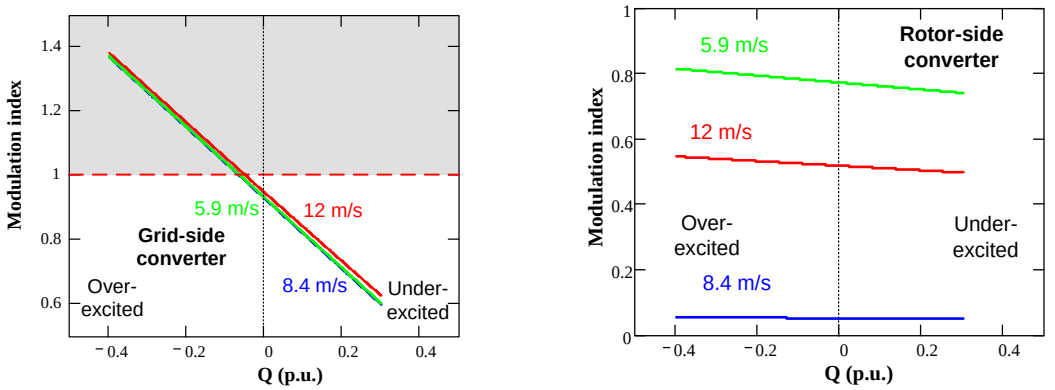

(a)

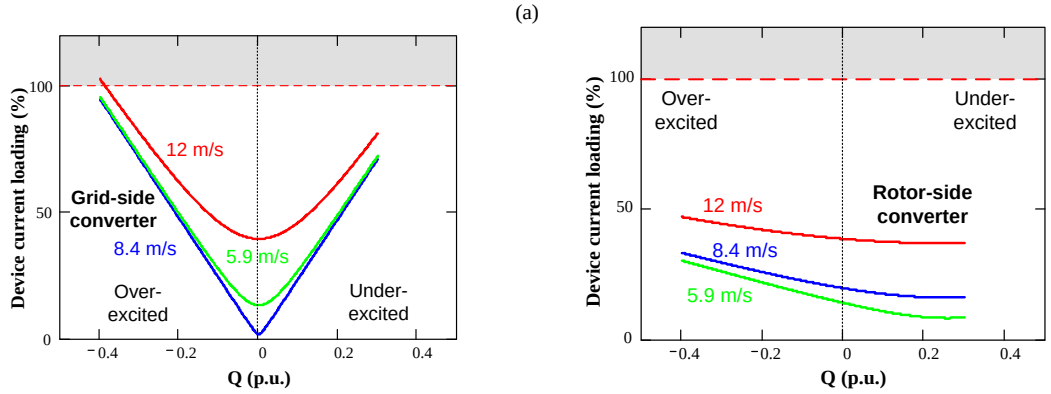

(b)

Fig. 13. Effects of the reactive power injection on the current and voltage stress of the power device. (a) Modulation index; (b) Device current loading.

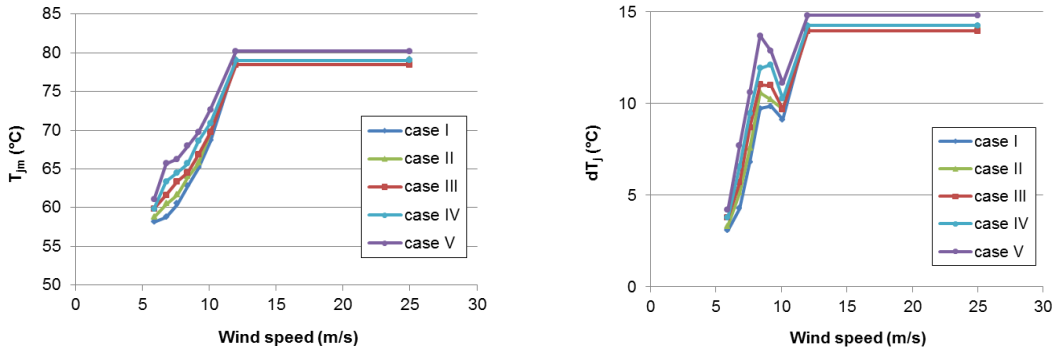

(a)

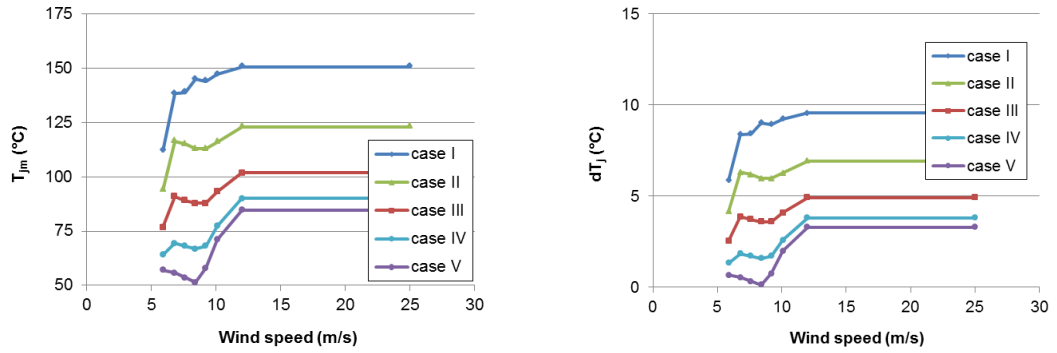

(b)

Fig. 14. Thermal profile of the most stressed power semiconductor in terms of the mean junction temperature and the junction temperature fluctuation, where the reactive power is provided with various compensation strategies. (a) Diode in the rotor-side converter; (b) IGBT in the grid-side converter.

because the over-excited or the under-excited reactive power introduces the same or opposite direction of voltage drop through the filter inductance in respect to the grid voltage as shown in Fig. 5. Furthermore, either the over-excited or under-excited reactive power considerably increases the current loading of the device.

For the RSC, as illustrated in (2) and (3), the rotor voltage is jointly decided by the stator and rotor winding ratio and slip value of the generator. As a result, the modulation index at different wind speeds are found in Fig. 13(a), in which the highest slip value causes the highest modulation index. In respect to the device loading of the RSC, the situation is also better than the GSC in the case of the reactive power injection. It is interesting to note that under-excited reactive power injection reduces the current stress of the power device, as under this circumstance, the excitation energy actually is supported by the grid. Because of the ratio between the stator winding and rotor winding of the induction generator, the variation of the current in each power device is also smaller than in the GSC. Above all, it is more effective to support the reactive power from the RSC compared to the GSC.

IV. JOINT REACTIVE POWER COMPENSATION FROM BTB POWER CONVERTER

As previously mentioned, the RSC and the GSC both have the abilities to support reactive power injection. This section will evaluate the effects of the reactive power flow between the GSC and the RSC seen from the lifetime and reliable operation point of view.

A. Different strategies for joint reactive power compensation

As the over-modulation affects the dynamic performance in the power electronics converter [31], [32], the different control strategies are all realized within the linear modulation range. As shown in Fig. 13, only the over-excited reactive power increases the current stress of the power device in the RSC, thus it will reduce the lifetime of the RSC. Different load sharing for the over-excited reactive power between the RSC and the GSC can be achieved by Table I, where the DC-voltage varies according to the linear modulation range of the GSC.

TABLE I

DIFFERENT STRATEGIES FOR JOINT REACTIVE POWER COMPENSATION

	RSC (pu)	GSC (pu)	U_{dc} (V)
Case I	0	-0.4	1500
Case II	-0.1	-0.3	1350
Case III	-0.2	-0.2	1200
Case IV	-0.3	-0.1	1100
Case V	-0.4	0	1050

Note: It is assumed that 0.4 pu over-excited reactive power is needed according to the grid codes [30].

B. Thermal behavior of the power semiconductor

According to (2) and (4), the different amounts of over-excited reactive power between the RSC and the GSC can be independently expressed by imaginary part of the stator current and the GSC output current. As a result, the conduction loss and the switching loss of the IGBT and the diode can be calculated. Moreover, substituting the loss information into (7) and (8), the most stressed power semiconductors for the BTB power converters (i.e. the freewheeling diode of the RSC and the IGBT of the GSC) are shown in Fig. 14(a) and Fig. 14(b).

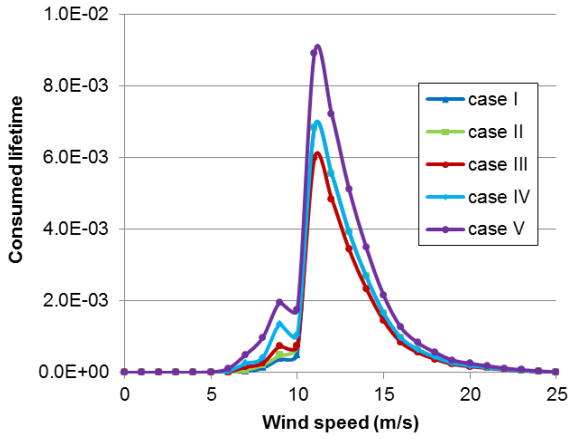

(a)

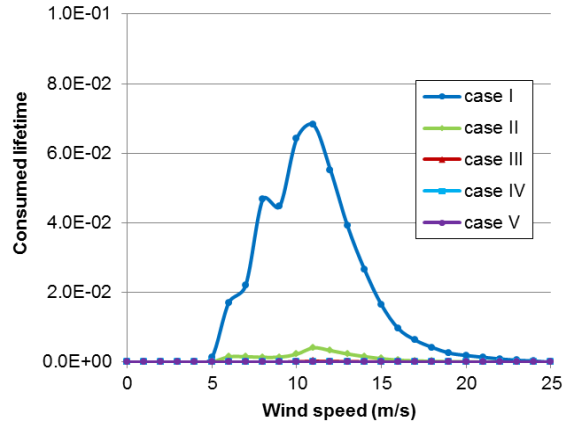

(b)

Fig. 15. Consumed lifetime of the most stressed power semiconductor at each wind speed. (a) Rotor-side converter; (b) Grid-side converter.

In Fig. 14(a), it can be seen that the mean junction temperature and the junction temperature fluctuation change insignificantly among all the compensation strategies. Meanwhile, the diode has the worst thermal behavior in Case V (reactive power fully compensated from the RSC), but has the best thermal performance in Case I (reactive power fully compensated from the GSC). In Fig. 14(b), the thermal performance of the IGBT in the GSC at different compensation strategies varies a lot. The worst situation is Case I (reactive power is fully supported by the GSC), in which the mean junction temperature almost reaches 150 ℃.

C. Lifetime trade-off between GSC and RSC

With the thermal profile of the most stressed power semiconductor shown in Fig. 14, as well as the fundamental frequency of the power converter output current and the annual wind speed distribution, the lifetime consumed per year of the individual wind speed is shown in Fig. 15. If the wind speed is above the rated value, it is obvious that the wind speed at 11 m/s has the highest consumed lifetime of the RSC. One of the reasons is that, as the rated wind speed is 11 m/s, the wind speed at 11 m/s has the highest percentage above the rated wind speed as shown in Fig. 9. The other factor is the same thermal performance above the rated wind speed as shown in Fig. 14(a). However, if the wind speed is below the rated value, although the 8 m/s wind speed (synchronous operation of the DFIG) hardly contains the highest percentage as shown in Fig. 9, it actually consumes the majority lifetime among the wind speeds below the rated value, owing to the fact that the synchronous operation has the largest junction temperature fluctuation below the rated wind speed as shown in Fig. 14(a). Moreover, the smaller amount of reactive power it injects from the RSC, the smaller consumed lifetime it can obtain.

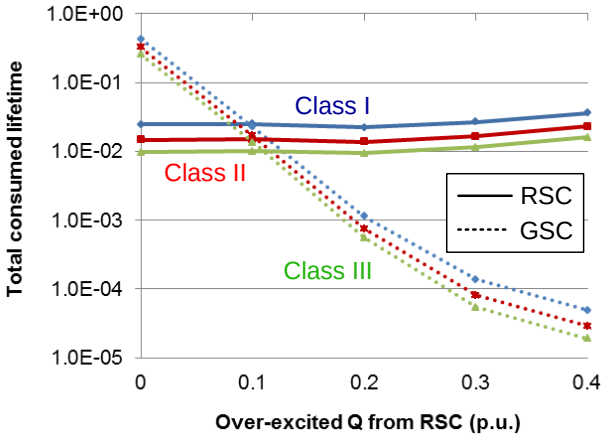

Fig. 16. Total consumed lifetime among the different compensation strategies, in which the various wind classes are also taken into account.

Note: a. The solid line indicates the diode of the rotor-side converter, and the dot line indicates the IGBT of the grid-side converter. b. Color blue, red and green indicate the wind Class I, Class II and Class III, respectively.

For the GSC, the lifetime consumed per year of the individual wind speed changes significantly with different compensation strategies. For instance, the highest consumed lifetime at 11 m/s moves from the worst 6.82E-2 in Case I to the best 1.42E-05 in Case V, which implies that the nearly 5000 times difference between them can easily induce the significant variation of the GSC lifetime.

The total consumed lifetime for the five combined reactive power strategies from the GSC and the RSC are shown in Fig. 16 using log scale, in which three wind classes are also considered. According to the IEC standard [33], [34], the mean wind speed of the Class I, Class II and Class III are 10 m/s, 8.5 m/s and 7.5 m/s, respectively. In the case of the wind Class I, the total consumed lifetime almost stays constant in a log-scale at different compensation schemes from the RSC point of view, while for the GSC, the total consumed lifetime varies significantly. Moreover, it can be seen that the most balanced lifetime between the RSC and the GSC appears in Case II, in which 0.1 pu over-excited reactive power is supported by the RSC and 0.3 pu is provided by the GSC. It is evident that the total consumed lifetime of the RSC can be optimized from 3.59E-2 (Case V) to 2.50E-2 (Case II), which implies 1.5 times enhanced lifespan. For different wind classes, the tendencies are almost consistent with the Class I wind.

V. EXPERIMENTAL RESULTS

In order to validate the equations and control strategies, a down-scale 7.5 kW test system has been built and is shown in Fig. 17. The DFIG is externally driven by a prime motor, and the power electronic converters are linked to the grid through an LCL filter. Two 5.5 kW Danfoss motor drives are used for the GSC and the RSC, both of which are controlled by the implementation of dSPACE 1006. Due to the fact that the junction temperature of the power semiconductor is not easy to be measured, the experimental results are conducted through the electrical characteristics of the DFIG system.

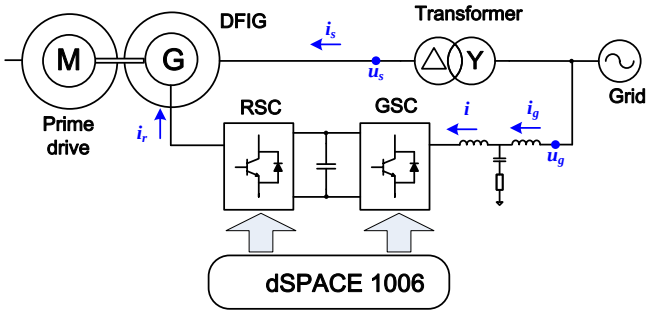

Fig. 17. Setup of the 7.5 kW DFIG system test rig.

With the parameters of the test system summarized in Appendix, the reactive power influence on the current and voltage stress of the BTB power converters are analytically calculated as shown in Fig. 18. It is noted that the tendency of the 7.5 kW DFIG system is similar to the 2 MW system as shown in Fig. 13 in terms of the modulation index as well as the current amplitude. Moreover, as the LCL filter significantly reduces the total inductance of the grid filter compared to the pure L structure filter, the DC-link of the test rig is set at 650 V and this value is high enough to supply 0.4 pu over-excited reactive power even from the GSC as shown in Fig. 18(a). Rotor speeds at 1050 rpm, 1470 rpm and 1800 rpm are selected for the sub-synchronous, synchronous and super-synchronous operations, whose produced active power are 1 kW, 3 kW and 5 kW, respectively. Then the modulation index and current amplitude can be tested at various amounts of the reactive power requirement.

As the loss of the induction generator can hardly be neglected in the 7.5 kW DFIG, an additional current is introduced in the BTB power converters to compensate the generator loss. As shown in Fig. 18(b), if no reactive power is

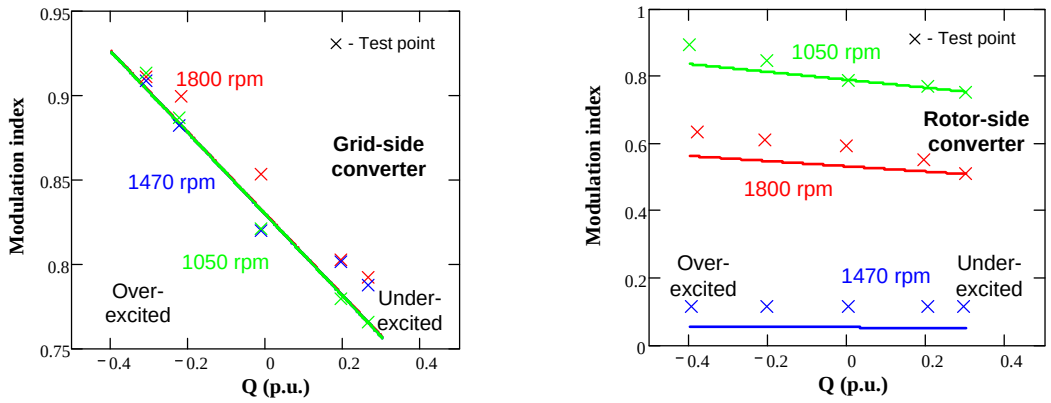

(a)

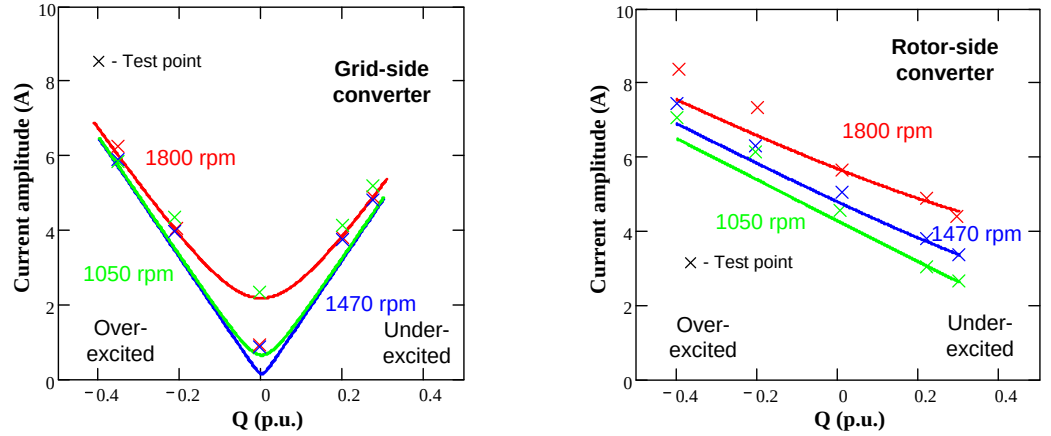

(b)

Fig. 18. Experimental validation of the reactive power influence on current and voltage stress of the back-to-back power converters. (a) Modulation index; (b) Device current loading.

Note: Active power references are 5 kW, 3 kW and 1 kW in the cases of the rotor speeds are 1800 rpm, 1470 rpm and 1050 rpm, respectively.

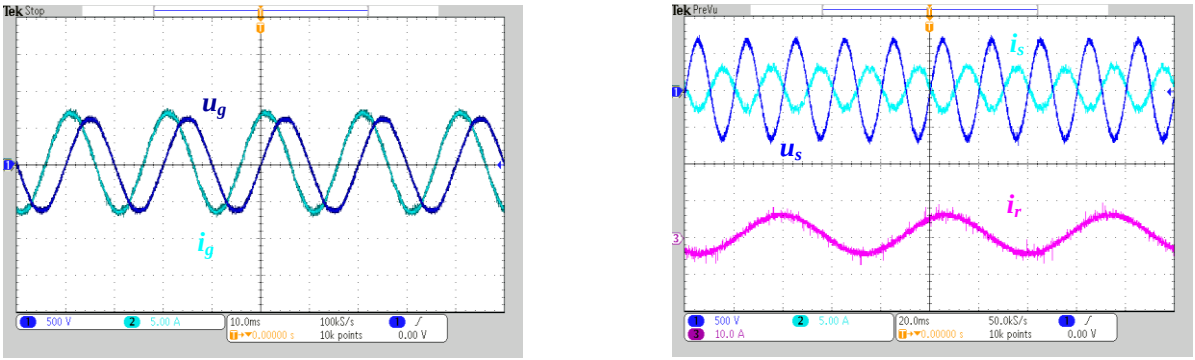

(a) (b)

Fig. 19. Experimental result of the DFIG test rig at the sub-synchronous speed of 1050 rpm if the 0.4 pu over-excited reactive power is fully injected by the grid-side converter. (a) Grid current in respect to the grid voltage; (b) Stator current and rotor current in respect to the stator voltage.

taken into account, the test result of the GSC is higher than the theoretical value at the sub-synchronous mode, while the current amplitude is a little lower than theoretical value at the super-synchronous mode. However, for the RSC, if no reactive power injection is considered, the tested rotor current amplitude is similar to the theoretical value because the active current component is rather small compared to the excitation current. Moreover, the tendencies of modulation index and current amplitude of the BTB power converters are consistent with the analytical values. Above all, it is concluded there is a good correlation between theory and experiment if the various amounts of the reactive power are taken into account.

Assuming the DFIG operates in the sub-synchronous mode at the 1050 rpm with 1 kW active power, the full amount of the over-excited reactive power 3 kVar can be provided by either the GSC or the RSC. As shown in Fig. 19, if the

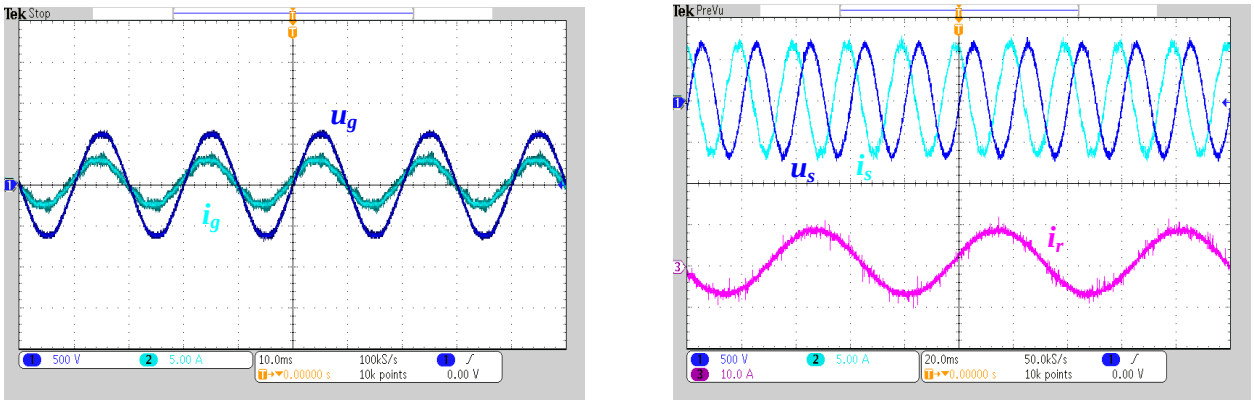

(a) (b)

Fig. 20. Experimental result of the DFIG test rig at the sub-synchronous speed of 1050 rpm if the 0.4 pu over-excited reactive power is fully injected by the rotor-side converter. (a) Grid current in respect to the grid voltage; (b) Stator current and rotor current in respect to the stator voltage.

reactive power compensation is fully provided by the GSC, the active current component could be rather small compared to the reactive current component due to the slip power flowing through. As a result, the GSC current is almost leading the grid voltage 90 degree. For the RSC, as the DFIG injects the power to the grid, the stator current and the stator voltage are almost reverse as expected.

Fig. 20 shows the case when the 0.4 pu over-excited reactive power is completely supported by the RSC. The GSC current is exactly in phase with the grid voltage, while the stator current is leading the stator voltage 90 degree due to the dominating reactive current component.

VI. CONCLUSION

In this paper, the consumed lifetime of the grid-side converter and the rotor-side converter in a DFIG system is firstly compared based on a typical annual wind profile. If there is no reactive power exchange between the DFIG and the grid, the grid-side converter has more than 100 times lifetime compared to the rotor-side converter due to their various control objectives and various fundamental frequencies of the output current.

The influence of the reactive power support required in the modern grid codes is also evaluated for the back-to-back power converters in terms of the modulation index and the current loading of the each device. It is found that the reactive power compensation from the rotor-side converter is more effective than the support from the grid-side converter. Moreover, it can also be seen that the over-excited reactive power significantly reduces the lifetime of the rotor-side converter.

By introducing an optimized reactive power flow between the grid-side converter and the rotor-side converter, the lifetime trade-off can be achieved, thus they have more balanced lifetime. It is concluded that, depending on the specific power converter design, the most appropriate reactive power division between the grid-side converter and the rotor-side converter can enhance the lifetime 1.5 times compared to the case that the reactive power is fully provided through the rotor-side converter. Furthermore, in order to enhance the reliability, a proper asymmetrical design of the back-to-back power converters as well as the chip re-design of the power device could also have a promising potential in design of the wind power converter.

APPENDIX

PARAMETERS FOR A 2 MW AND 7.5 KW DFIG

DFIGs		
Rated power P_n [kW]	2000	7.5
Phase peak voltage U_{sn} [V]	563	311
Stator resistance R_s [mΩ/pu]	1.69/0.007	440/0.023
Stator leakage inductance L_{ls} [mH/pu]	0.04/0.050	3.44/0.056
Rotor resistance R_r [mΩ/pu]	1.52/0.006	640/0.033
Rotor leakage inductance L_{lr} [mH/pu]	0.06/0.085	5.16/0.085
Magnetizing inductance L_m [mH/pu]	2.91/3.840	79.30/1.294
Turns ratio N_s/N_r	0.369	0.336
Power converters		
Rated power [kW]	400	5
DC-link voltage U_{dc} [V/pu]	1050/1.522	650/1.711
Switching frequency f_s [kHz]	2	5
Grid filters		
Boost inductance [mH/pu]	0.5/0.132	18/0.039*

"*" indicates the total inductance of the LCL filter, including both the grid-side inductor and the converter-side inductor.

REFERENCES

[1] "World wind energy association – 2013 half-year report". (Available at: http://www.wwindea.org/home/index.php).

[2] Y. Li, L. Luo, C. Rehtanz, C. Wang, and S. Ruberg, "Simulation of the electromagnetic response characteristic of an inductively filtered HVDC converter transformer using field-circuit coupling," *IEEE Trans. Ind. Electron.* , vol. 59, no. 11, pp. 4020-4031, Nov. 2012.

[3] F. Blaabjerg, Z. Chen, and S. B. Kjaer, "Power electronics as efficient interface in dispersed power generation systems," *IEEE Trans. Power Electron.*, vol. 19, no. 5, pp. 1184-1194, Sep. 2004.

[4] J. M. Carrasco, L. G. Franquelo, J. T. Bialasiewicz, E. Galvan, R. C. P. Guisado, Ma. A. M. Prats, J. I. Leon, and N. Moreno-Alfonso, "Power-electronic systems for the grid integration of renewable energy sources: a survey," *IEEE Trans. Ind. Electron.*, vol. 53, no. 4, pp. 1002-1016, Jun. 2006.

[5] J. M. Guerrero, F. Blaabjerg, T. Zhelev, K. Hemmes, E. Monmasson, S. Jemei, M. P. Comech, R. Granadino, and J. I. Frau, "Distributed generation: toward a new energy paradigm," *IEEE Ind. Electron. Mag.*, vol. 4, no. 1, pp. 52-64, Mar. 2010.

[6] M. Liserre, R. Cardenas, M. Molinas, and J. Rodriguez, "Overview of multi-MW wind turbines and wind parks," *IEEE Trans. Ind. Electron.*, vol. 58, no. 4, pp. 1081-1095, Apr. 2011.

[7] B. Hahn, M. Durstewitz, and K. Rohrig "Reliability of wind turbines - Experience of 15 years with 1500 WTs," *Wind Energy: Proceedings of the Euromech Colloquium*, pp. 329-332, Springer-Verlag, Berlin.

[8] ZVEL, Handbook for robustness validation of automotive electrical/electronic modules, Jun. 2008.

[9] D. Hirschmann, D. Tissen, S. Schroder, and R.W. De Doncker, "Inverter design for hybrid electrical vehicles considering mission profiles," *in Proc. of IEEE Conference Vehicle Power and Propulsion 2005*, pp. 1-6, 2005.

[10] C. Busca, R. Teodorescu, F. Blaabjerg, S. Munk-Nielsen, L. Helle, T. Abeyasekera, and P. Rodriguez, "An overview of the reliability prediction related aspects of high power IGBTs in wind power applications," *Microelectronics Reliability*, vol. 51, no. 9-11, pp. 1903-1907, 2011.

[11] S. Yang, A. Bryant, P. Mawby, D. Xiang, L. Ran, and P. Tavner, "An industry-based survey of reliability in power electronic converters," *IEEE Trans. Ind. Appl.*, vol. 47, no. 3, pp. 1441-1451, May-June 2011.

[12] F. Richardeau, and T. T. L. Pham, "Reliability calculation of multilevel converters: theory and applications," *IEEE Trans. Ind. Electron.*, vol. 60, no. 10, pp. 4225-4233, Oct. 2013.

[13] H. Behjati, and A. Davoudi, "Reliability analysis framework for structural redundancy in power semiconductors," *IEEE Trans. Ind. Electron.*, vol. 60, no. 10, pp. 4376-4386, Oct. 2013.

[14] ABB Application Note, Load-cycling capability of HiPaks, 2004.

[15] A. Wintrich, U. Nicolai, and T. Reimann, "Semikron Application Manual," p. 128, 2011.

[16] U. Scheuermann, and R. Schmidt, "A new lifetime model for advanced power modules with sintered chips and optimized Al wire bonds", *in Proc. of PCIM 2013*, pp. 810-813, 2013.

[17] K. Ma, M. Liserre, F. Blaabjerg, and T. Kerekes, "Thermal loading and lifetime estimation for power device considering mission profiles in wind power converter," *IEEE Trans. Power Electron.*, IEEE early access.

[18] D. Weiss, and H. Eckel, "Fundamental frequency and mission profile wearout of IGBT in DFIG converters for windpower", *in Proc. of EPE 2013*, pp. 1-6, 2013.

[19] H. Wang, M. Liserre, and F. Blaabjerg, "Toward reliable power electronics: challenges, design tools, and opportunities," *IEEE Ind. Electron. Mag.*, vol. 7, no. 2, pp. 17-26, Jun. 2013.

[20] H. Wang, D. Zhou, and F. Blaabjerg, "A reliability-oriented design method for power electronic converters," *in Proc. of APEC 2013*, pp. 2921-2928, 2013.

[21] B. Cezar Rabelo, W. Hofmann, J. L. da Silva, R. G. de Oliveira, and S. R. Silva, "Reactive power control design in doubly fed induction generators for wind turbines," *IEEE Trans. Ind. Electron.*, vol. 56, no. 10, pp. 4154-4162, Oct. 2009.

[22] D. P. Bagarty, and D. Kastha, "Reactive power allocation for loss minimization in a stand-alone variable speed constant frequency double output induction generator," *IET Power Electronics*, vol. 6, no. 5, pp. 851-861, May 2013.

[23] T. B. Soeiro, and J. W. Kolar, "Analysis of high-efficiency three-phase two- and three-level unidirectional hybrid rectifiers," *IEEE Trans. Ind. Electron.*, vol. 60, no. 9, pp. 3589-3601, Sep. 2013.

[24] D. Zhou, F. Blaabjerg, M. Lau, and M. Tonnes, "Thermal analysis of multi-MW two-level wind power converter," *in Proc. of IECON 2012*, pp. 5862-5868, 2012.

[25] K. Zhou, and D. Wang, "Relationship between space-vector modulation and three-phase carrier-based PWM: a comprehensive analysis," *IEEE Trans. Ind. Electron.*, vol. 49, no. 1, pp. 186-196, Feb. 2002.

[26] D. Zhou, F. Blaabjerg, M. Lau, and M. Tonnes, "Thermal cycling overview of multi-megawatt two-level wind power converter at full grid code operation," *IEEJ Journal of Industry Applications*, vol. 2, no. 4, pp. 173-182, Jul. 2013.

[27] M. Marz, and P. Nance, "Thermal modeling of power-electronic system". (Available at: http://www.infineon.com/)

[28] D. Zhou, F. Blaabjerg, M. Lau, and M. Tonnes, "Thermal profile analysis of doubly-fed induction generator based wind power converter with air and liquid cooling methods," *in Proc. of EPE 2013*, pp.1-10, 2013.

[29] M. A. Miner, "Cumulative damage in fatigue," *Journal of Applied Mechanics*, no. 12, A159-A164, 1945.

[30] E.ON-Netz. Requirements for offshore grid connections, Apr. 2008.

[31] D. Zhou, F. Blaabjerg, M. Lau, and M. Tonnes, "Thermal behavior optimization in multi-MW wind power converter by reactive power circulation," *IEEE Trans. Ind. Appl.*, vol. 50, no. 1, pp. 433-440, Jan. 2014.

[32] S. Busquets-Monge, R. Maheshwari, and S. Munk-Nielsen, "Over-modulation of n-level three-leg DC–AC diode-clamped converters with comprehensive capacitor voltage balance," *IEEE Trans. Ind. Electron.*, vol. 60, no. 5, pp. 1872-1883, May 2013.

[33] "Wind turbines – part I: design requirements", IEC 61400-1, 3rd edition.

[34] Vestas website (Available at: http://www.vestas.com/en/wind-power-plants/wind-project-planning/siting/wind-classes.aspx?action=3#/vestas-univers).

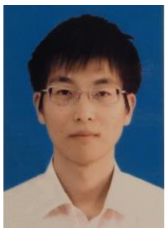

Dao Zhou (S'12) received the B.Sc. in electrical engineering from Beijing Jiaotong University, Beijing, China, in 2007, and the M. Sc. in power electronics from Zhejiang University, Hangzhou, China, in 2010. From 2012, he is pursuing the Ph.D degree in the Department of Energy Technology, Aalborg University, Aalborg, Denmark.

His research interests include two-level power electronics converters and their application in wind power generation systems.

Frede Blaabjerg (S'86-M'88-SM'97-F'03) was with ABB-Scandia, Randers, Denmark, from 1987 to 1988. From 1988 to 1992, he was a PhD student with Aalborg University, Aalborg, Denmark. He became an Assistant Professor in 1992, an Associate Professor in 1996, and a Full Professor of power electronics and drives in 1998. His current research interests include power electronics and its applications such as in wind turbines, PV systems, reliability, harmonics and adjustable speed drives.

He has received 15 IEEE Prize Paper Awards, the IEEE PELS

Distinguished Service Award in 2009, the EPE-PEMC Council Award in 2010, the IEEE William E. Newell Power Electronics Award 2014 and the Villum Kann Rasmussen Research Award 2014. He was an Editor-in-Chief of the IEEE TRANSACTIONS ON POWER ELECTRONICS from 2006 to 2012. He has been Distinguished Lecturer for the IEEE Power Electronics Society from 2005 to 2007 and for the IEEE Industry Applications Society from 2010 to 2011.

Mogens Lau received the M.Sc. in Electrical engineering from Aalborg University, Aalborg, Denmark, in 1999. He worked as development engineer, project manager and line manager within power electronics at leading companies like Siemens, Danfoss, Grundfoss and Vestas. Currently, he is the working with Siemens Wind Power A/S in Brande, Denmark.

Michael Tonnes received the M.Sc. EE degree from Aalborg University, Denmark in 1987, and the Ph.D. degree from the Institute of Energy Technology in 1990.

He was employed by Danfoss in 1987 to perform the Ph.D work within auto-tuning and automatic control of non-linear electrical machines and worked within the technology area of Motor Controls. Michael worked in US in Danfoss High Power Drives for the period 1996-98 and had various management positions within electronic businesses. At present he is Senior Director of R&D at Danfoss Silicon Power GmbH with base in Flensburg, Germany.

He is author and co-author on a number of articles within auto-tuning, motor controls and power electronics in general and holds several patents within the field motor controls and power electronics.